Proceedings of Meetings on Acoustics

Volume 14, 2011 http://acousticalsociety.org/

162nd Meeting
Acoustical Society of America
San Diego, California
31 October - 4 November 2011
Session 4pEA: Engineering Acoustics

4pEA8. Capacity and Statistics of Measured Underwater Acoustic Particle Velocity Channels

Huaihai Guo, Chen Chen, Ali Abdi*, Aijun Song, Mohsen Badiey and Paul Hursky

***Corresponding author's address: Electrical and Computer Engineering, New Jersey Institute of Technology, 323 M.L.King Blvd, Newark, NJ 07102, ali.abdi@njit.edu**

Acoustic particle velocity channels can be used for communication in underwater systems [A. Abdi and H. Guo, IEEE Trans. Wireless Communi. 8, 3326-3329, (2009)]. In this paper, the information (Shannon) capacity of underwater acoustic particle velocity channels is studied using measured data. More specifically, the maximum achievable data rates of a compact vector sensor communication receiver and another communication receiver with spatially separated scalar sensors are compared. Some statistics of particle velocity channels such as amplitude distribution and power delay profile are investigated using measured data and proper models are suggested as well. The results are useful for design and simulation of vector sensor underwater communication systems in particle velocity channels.The work is supported in part by the National Science Foundation (NSF), Grant CCF-0830190.

Published by the Acoustical Society of America through the American Institute of Physics

 [DOI: 10.1121/1.4704639]
Received 3 Feb 2012; published 3 Apr 2012

I. INTRODUCTION

Communication via acoustic particle velocity channels using vector sensors has been recently proposed for underwater systems [1][2]. In addition to the acoustic pressure channel [3][4], acoustic particle velocity channels provide extra channels for communication [5]. Experimental results have shown the usefulness of such channels for communication [6]. Some statistical characteristics of particle velocity channels are investigated in [7] and [8]. The interested reader can refer to [5] for a summary of channel modeling and communication system design research in particle velocity channels.

The information capacity of underwater acoustic pressure channels is studied in a number of publications, e.g., [9]-[13]. In this paper, we use experimental data to study the capacity offered by a multi-channel vector sensor receiver that measures the x, y and z components of the acoustic particle velocity, as well as the acoustic pressure. The capacity provided by a receive array with four spatially separated scalar pressure sensors is investigated as well, using the collected data. As a benchmark, capacity of a four channel receiver in Rayleigh fading is also calculated. Measured capacities of both the vector sensor receiver and the scalar array receiver are compared with this Rayleigh capacity reference, to obtain further insight. Amplitude distributions of the measured acoustic particle velocity and pressure channels are also compared with Rayleigh distribution, to study the suitability of the Rayleigh model.

The rest of the paper is organized as follows. The measured data and experiment setup are explained in Section II. In Section III narrowband capacities of the vector sensor receiver and the scalar array receiver are considered, whereas Section IV is devoted to wideband capacities. Concluding remarks are provided in Section V.

II. AT-SEA EXPERIMENTS AND MEASURED DATA

A multi-channel vector sensor communication receiver is shown in Fig. 1. There we have one transmit scalar (pressure) sensor, the black sphere, and a vector sensor receiver, the black cube which measures signals in pressure, x, y and z particle velocity channels. Therefore, this is a

1×4 single-input multiple-output (SIMO) communication system.

The data sets analyzed in this paper were collected during the Makai experiment in Hawaii in September and October of 2005 [14]. The water depth at the site was about 100m. A high frequency sound source was mounted on the sea floor. A Wilcoxon TV-001 vector sensor array was hung from the research vessel, with the bottom element at the nominal depth of 40m. The element spacing was 10cm. The fifth, or the bottom, element did not function properly during the experiment. Each vector sensor element measured pressure, as well as *x*, *y* and *z* velocities. During the experiment, the array was considered vertical since a 200 lbs. weight was attached to the end of the array.

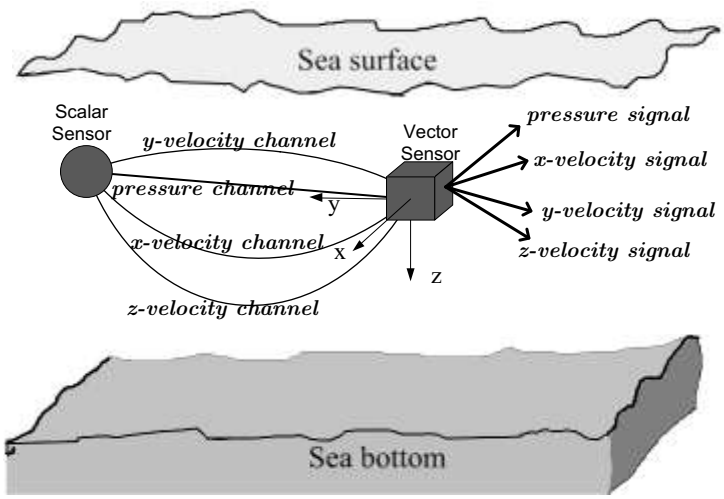

Fig. 1 A 1×4 vector sensor communication system with one pressure sensor transmitter. The vector sensor receiver measures the acoustic pressure, as well as the *x*, *y* and *z* components of the acoustic particle velocity, all at a single point.

Impulse responses of the channels from scalar sensor transmitter to a four-channel vector sensor receiver were measured, as well as those between the transmitter and four scalar sensor receivers. A binary phase shift keying (BPSK) signal with a symbol rate of 6 kilo-symbols/second was used to probe the impulse responses, at the carrier frequency of f_c = 12 kHz. At the transmit side, the pressure sensor sent out a 3.5-second-long data packet which contained 54 sequences. At the receiver side, the received signals were transformed to the baseband and

then were fractionally sampled at the rate of 3 samples/symbol. Therefore, the sampling rate of the baseband signal was 18 kHz. Then a 25ms-long channel impulse response was estimated using the least square method. In this paper, the experimental data collected for the communication range of 900 m are analyzed. For example, magnitude of the measured channel impulse response during the 3.5 second packet for the *x*-velocity channel, $|h^x[n,l]|$, is shown in Fig. 2, where n and l stand for the geotime and arrival time, respectively. Magnitudes of normalized (unit-power) impulse responses of the pressure channel as well as x, y and z velocity channels are shown in Fig. 3. Frequency response of each channel is obtained by taking the Fourier transform of the corresponding channel impulse response. Magnitudes of the frequency responses of the channels in Fig. 3 are shown in Fig. 4.

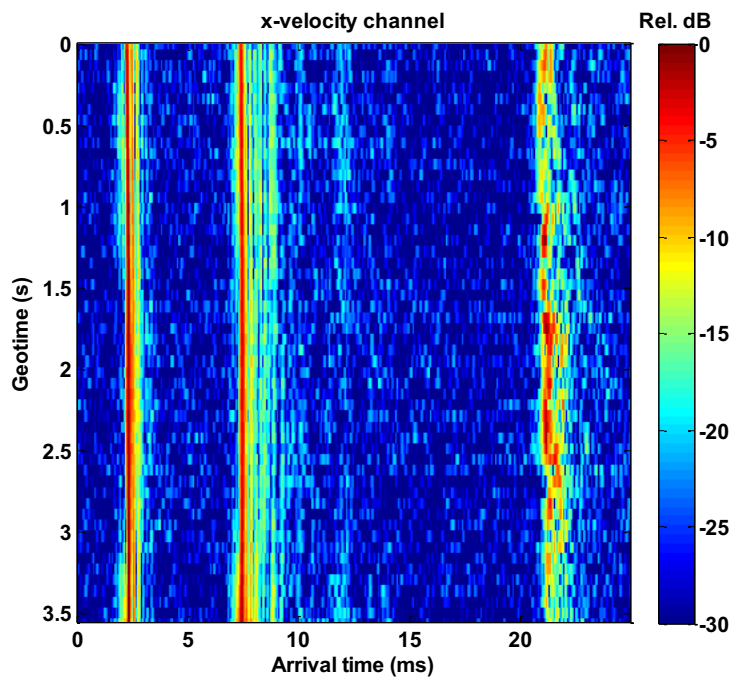

Fig. 2 Measured impulse response of the *x*-velocity channel.

Magnitudes of normalized (unit-power) temporal correlation functions of the pressure channel, as well as *x*, *y* and *z* velocity channels are shown in Fig. 5. Similarly to [15] and [16], the temporal correlation function for a channel is defined as $\phi[\Delta n] = E\{h^*[n]h[n+\Delta n]\}$ where E

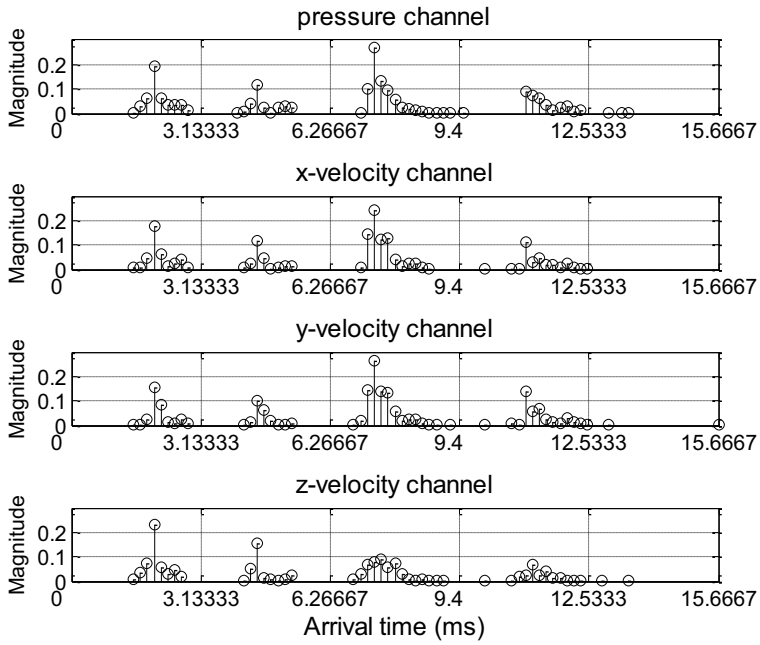

Fig. 3 Magnitudes of average unit power vector sensor channel impulse responses at 900m.

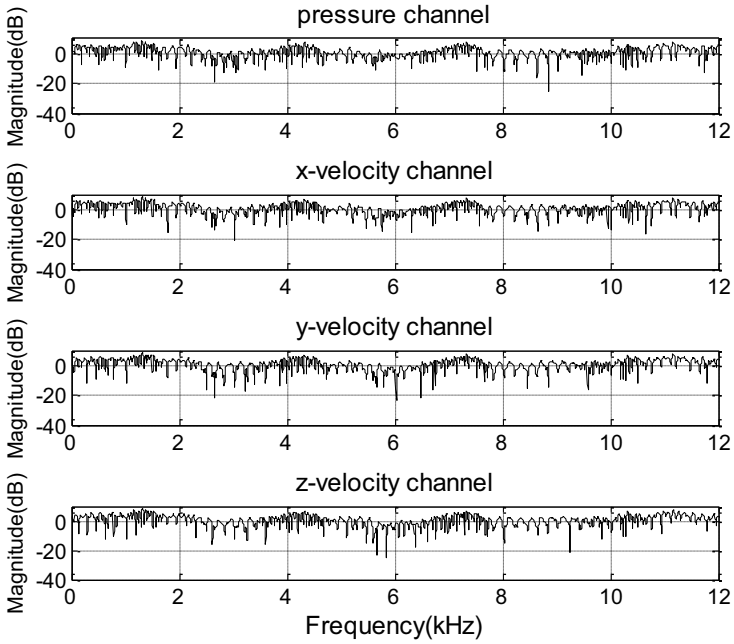

Fig. 4 Magnitudes of average vector sensor frequency responses at 900m.

is mathematical expectation, * is complex conjugate, and $h[n]$ is the zero-mean unit variance complex channel response. Note that $h[n]$ is related to the channel impulse response $h[n,l]$

according to $h[n]=\sum_{l=0}^{\infty}h[n,l]$. By looking at the frequency domain [15], one can see $h[n]$ is the time-varying narrowband channel response, where the signal bandwidth is much smaller than the channel bandwidth. On the other hand, $h[n,l]$ is the time-varying wideband channel response, where the signal bandwidth is much larger than the channel bandwidth. These two correspond to frequency-nonselective and frequency-selective channels, respectively [15].

Coherence time T_c of a time-varying channel is the interval over which the channel remains nearly constant [15]. Using the -3 dB point of the temporal correlation function [16] [17], coherence times of the pressure and particle velocity channels are about 700 ms. On the other hand, our signaling rate is $1/T=6$ kilo-symbols/second, which indicates $T\approx 0.17$ ms. Therefore, one can say our channels are nearly time-invariant because $T \ll T_c$ [15] [17]. Note that the length of the probe signal, 25 ms, is much smaller than $T_c \approx 700$ ms as well. So, the pressure and particle velocity channels can be considered to be time-invariant during short signaling intervals of interest. This allows to compute capacity using at-sea measured data, similarly to other underwater channel capacity studies such as [12], [13], [16], [18], etc.

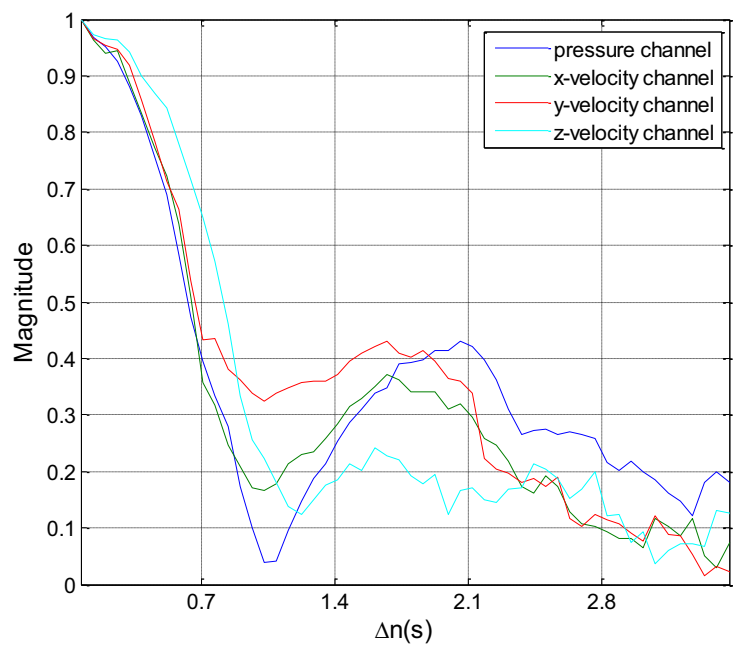

Fig. 5 Magnitudes of average unit power vector sensor temporal correlation functions at 900m.

III. NARROWBAND CHANNEL CAPACITY

In this section we study the narrowband channel capacity of the 1×4 SIMO communication system with a vector sensor receiver. Let **x** and **y** denote the $M_T \times 1$ transmitted signal vector and the $M_R \times 1$ received signal vector, respectively, of an $M_T \times M_R$ multiple-input multiple-output (MIMO) system. Then the narrowband input-output system equation is

$$\mathbf{y} = \mathbf{H}\mathbf{x} + \mathbf{v}, \tag{1}$$

where **H** is the narrowband $M_R \times M_T$ complex channel response matrix with elements h_{ij}, $i = 1, \cdots, M_R$ and $j = 1, \cdots, M_T$, and **v** is the $M_R \times 1$ additive noise vector. The capacity of this system, when channel is known at the receiver, is given by [19]

$$C = \log_2\left[1 + \rho \mathbf{H}^H \mathbf{H}\right], \tag{2}$$

where $\log_2$ is logarithm to the base 2 and $\rho = \Omega_{signal} / \Omega_{noise}$ is the signal-to-noise ratio (SNR) , with Ω_{signal} as the average signal power and Ω_{noise} as the average noise power at every receive channel, respectively. Moreover, $(\cdot)^H$ is transpose conjugate. In this paper we have $M_T = 1$, $M_R = 4$ and therefore $\mathbf{H} = [h_{11}\ h_{21}\ h_{31}\ h_{41}]^T$, where $(\cdot)^T$ is matrix transpose. In the vector sensor receiver, h_{11}, h_{21}, h_{31} and h_{41} represent the pressure, *x*-velocity, *y*-velocity and *z*-velocity channels , respectively. In the scalar array receiver, h_{11} corresponds to the scalar pressure sensor at the top of the array, whereas h_{41} corresponds to the one at the bottom of the array.

A. Narrowband Channel Response Distribution

The cumulative distribution function (CDF) of the narrowband channel amplitude $r[n] = |h[n]|$ is shown in Fig. 6 and Fig. 7 for the vector sensor and scalar array receivers, respectively, using 54 channel measurements. The unit power Rayleigh CDF $1 - e^{-r^2}$ is plotted in both figures as a reference, and appears to be close to the empirical CDFs.

B. Narrowband Channel Capacity

Using eq. (2), the average capacity of the vector sensor receiver is plotted in Fig. 8, based on measured data, as well as the capacity of the scalar array receiver. The two receivers provide nearly the same capacity. As a reference, the average capacity of a 1×4 system in narrowband

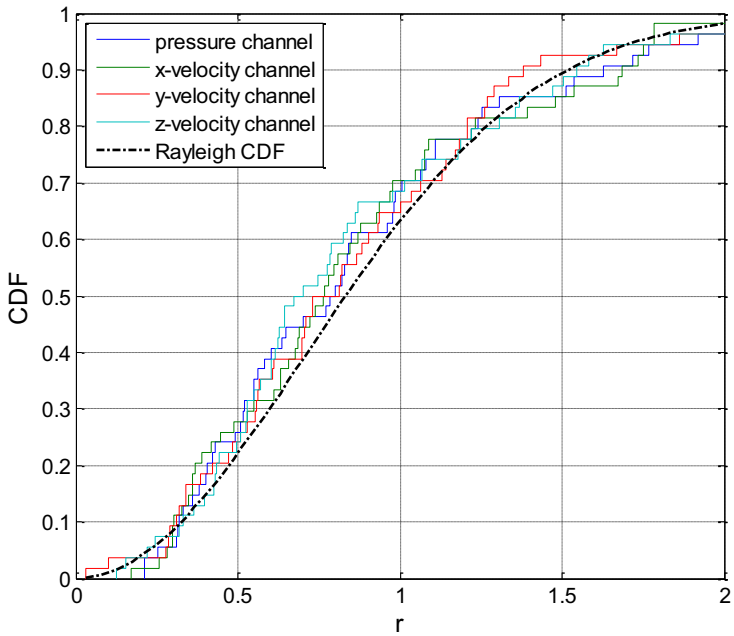

Fig. 6 CDFs of the amplitudes of narrowband responses of different channels in a vector sensor receiver at 900m.

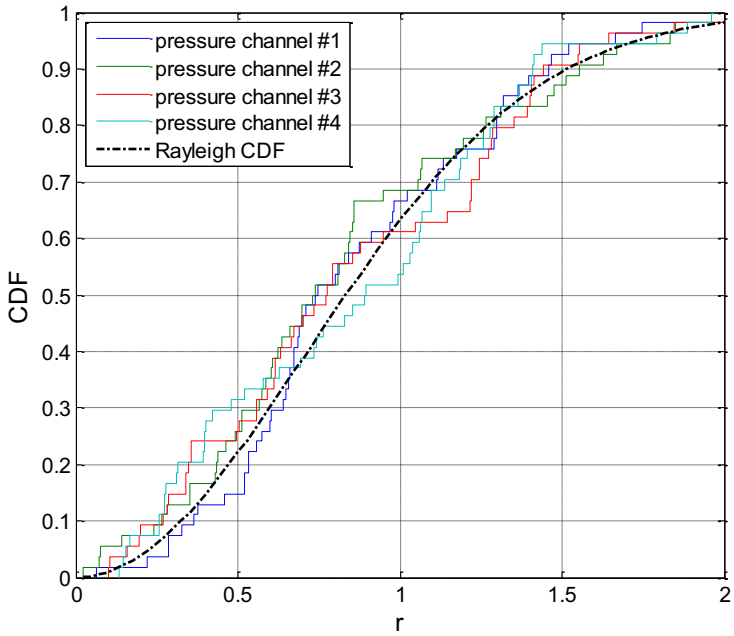

Fig. 7 CDFs of the amplitudes of narrowband responses of different channels in a four-element scalar array receiver at 900m.

Rayleigh fading is also plotted in Fig. 8, which appears to be a good model for measured capacities. Rayleigh capacity can be calculated using either [20]

$$\bar{C} = \frac{1}{6}\int_0^{\infty} \log_2(1+\rho\xi)\xi^3 e^{-\xi} d\xi \,, \tag{3}$$

or eq. (34) in [21]

$$\bar{C} = \frac{1}{\ln 2}\sum_{i=1}^{4}\int_1^{\infty} e^{-(\xi-1)/\rho} / \xi^{5-i}\, d\xi \,, \tag{4}$$

where $\ln$ is natural logarithm to the base e.

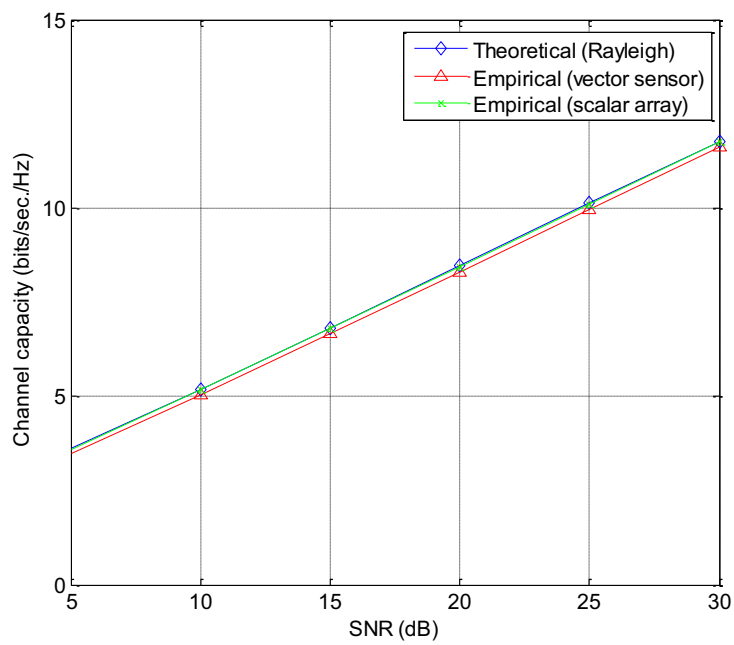

Fig. 8 Narrowband channel capacities at 900m.

IV. WIDEBAND CHANNEL CAPACITY

The wideband channel capacity of the 1×4 SIMO communication system with a vector sensor receiver is studied in this section. The general wideband MIMO system equation with L channel taps is given by

$$\mathbf{y}[n] = \sum_{l=0}^{L-1} \mathbf{H}_l \mathbf{x}[n-l] + \mathbf{v}[n], \tag{5}$$

where $\mathbf{H}_l$ is an $M_R \times M_T$ complex matrix that represents the lth tap of the MIMO channel response. By applying N-point discrete Fourier transform (DFT) to both sides of (5), we obtain

the system equations in the frequency domain

$$\tilde{\mathbf{y}}_k = \tilde{\mathbf{H}}_k \tilde{\mathbf{x}}_k + \tilde{\mathbf{v}}_k,\ k = 0, 1, \cdots N-1. \tag{6}$$

Here $\tilde{\mathbf{H}}_k = \sum_{l=0}^{L-1} \mathbf{H}_l e^{-j2\pi lk/N}$ is the $M_R \times M_T$ frequency domain channel matrix in the kth frequency bin, whereas $\tilde{\mathbf{y}}_k$, $\tilde{\mathbf{x}}_k$ and $\tilde{\mathbf{v}}_k$ are frequency domain representations of the received signal vector, transmitted signal vector and noise vector in the kth bin, respectively. The capacity of this system with channel known at the receiver is given by [22]

$$C = \frac{1}{N} \sum_{k=0}^{N-1} \log_2 \left[\det\left(\mathbf{I}_{M_R} + \rho \tilde{\mathbf{H}}_k \tilde{\mathbf{H}}_k^H \right) \right], \tag{7}$$

where $\rho = \Omega_{signal} / (N\tilde{\Omega}_{noise})$ is the SNR per receive channel, with Ω_{signal} as the average signal power and $\tilde{\Omega}_{noise}$ as the average noise power per receive channel per frequency bin.

A. Power Delay Profile

Power delay profile (PDP) is an important characteristic of wideband channels, as it shows the distribution of power at different delays [23]. It is the basis of the wideband channel capacity simulation. Here we consider the multi-exponential PDP model [23]

$$\Gamma[l] = \sum_{m=1}^{M} \gamma_m \exp[-\beta_m (l - l_m)], \tag{8}$$

where γ_m, β_m and l_m are the weight, decay rate and position of the mth one-side exponential (cluster), respectively.

In Fig. 9a, the empirical PDPs of all channels of the vector sensor receiver are shown, such that each PDP is normalized to have unit area. According to this figure there are $M = 4$ clusters in each channel. Upon choosing l_m's from Fig. 9a, the parameters γ_m and β_m are estimated using a numerical least-squares method, which are

$$\boldsymbol{\gamma}^{VS} = \begin{bmatrix} 0.1581 & 0.0571 & 0.0850 & 0.0391 \\ 0.1452 & 0.0535 & 0.0941 & 0.0735 \\ 0.0930 & 0.0392 & 0.1143 & 0.0912 \\ 0.2003 & 0.0927 & 0.0474 & 0.0330 \end{bmatrix},$$

$$\boldsymbol{\beta}^{VS} = \begin{bmatrix} 0.4680 & 0.4736 & 0.2871 & 0.4251 \\ 0.4443 & 0.4287 & 0.3153 & 0.9173 \\ 0.3846 & 0.3296 & 0.2990 & 0.7562 \\ 0.4708 & 0.4797 & 0.3760 & 0.3506 \end{bmatrix}, \tag{9}$$

$$\mathbf{l}^{VS} = \begin{bmatrix} 11 & 26 & 43 & 66 \\ 11 & 26 & 43 & 66 \\ 11 & 26 & 43 & 66 \\ 11 & 26 & 44 & 66 \end{bmatrix}.$$

The superscripts ^{VS} in (9) stands for vector sensor and each mth column corresponds to the mth cluster. Moreover, rows from top to bottom in each matrix correspond to the pressure, x-velocity, y-velocity and z-velocity channels, respectively. Using the estimated parameters, multi-exponential PDP models of all the channels in the vector sensor are plotted in Fig. 9b, which closely mimic the empirical PDPs.

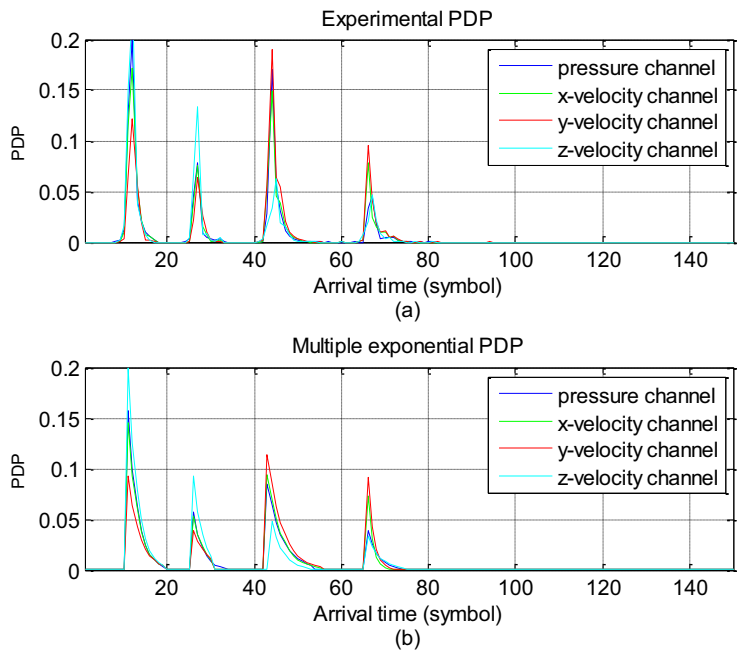

Fig. 9 Power delay profiles of a vector sensor receiver: (a) Estimated directly from measured data, (b) Multi-exponential model with parameters estimated from measured data.

The empirical PDPs of all the channels of the scalar array (SA) receiver are shown in Fig. 10a, and the corresponding estimated multi-exponential PDP models are presented in Fig. 10b,

where the parameters are

$$\boldsymbol{\gamma}^{SA} = \begin{bmatrix} 0.1782 & 0.0671 & 0.0808 & 0.0410 \\ 0.1879 & 0.0744 & 0.0727 & 0.0266 \\ 0.2020 & 0.0829 & 0.0774 & 0.0322 \\ 0.2077 & 0.0886 & 0.0641 & 0.0283 \end{bmatrix},$$

$$\boldsymbol{\beta}^{SA} = \begin{bmatrix} 0.5381 & 0.5713 & 0.3341 & 0.3313 \\ 0.5426 & 0.5643 & 0.3442 & 0.2008 \\ 0.5785 & 0.6147 & 0.4909 & 0.2056 \\ 0.5498 & 0.5709 & 0.4504 & 0.2238 \end{bmatrix}, \tag{10}$$

$$\mathbf{l}^{SA} = \begin{bmatrix} 14 & 29 & 46 & 68 \\ 14 & 29 & 46 & 67 \\ 14 & 29 & 47 & 67 \\ 14 & 29 & 47 & 67 \end{bmatrix}.$$

Similarly to eq.(9), in each of the above matrices the mth column represents the mth cluster, whereas the first and last rows correspond to the scalar sensors at the top and bottom of the array, respectively.

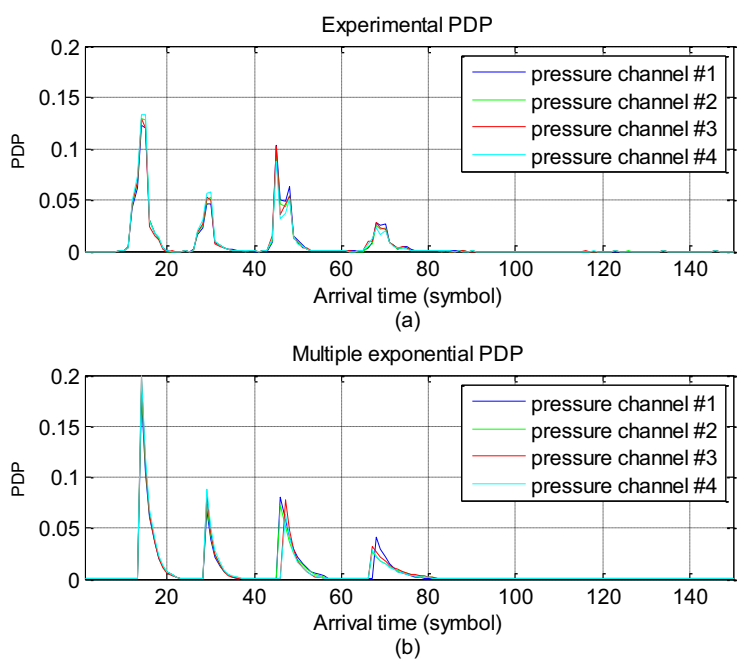

Fig. 10 Power delay profile of a scalar array receiver: (a) Estimated directly from measured data, (b) Multi-exponential model with parameters estimated from measured data.

B. Wideband Channel Response Distribution

As shown in Fig. 9 and Fig. 10, there are four channel taps with the maximum power in four clusters. Since these taps contribute the most to the received power, here we study their amplitude distributions. Experimental CDFs of these channel taps are shown in Fig. 11 and Fig. 12 for the vector sensor receiver and the scalar array receiver, respectively. The unit power Rayleigh CDF $1-e^{-r^2}$ is also shown in these figures, the dashed curve labeled with "R". As expected, we observe some deviations from Rayleigh distribution compared to the narrowband case. This is because the number of multipath components in some taps might be small and therefore central limit theorem is less likely to hold.

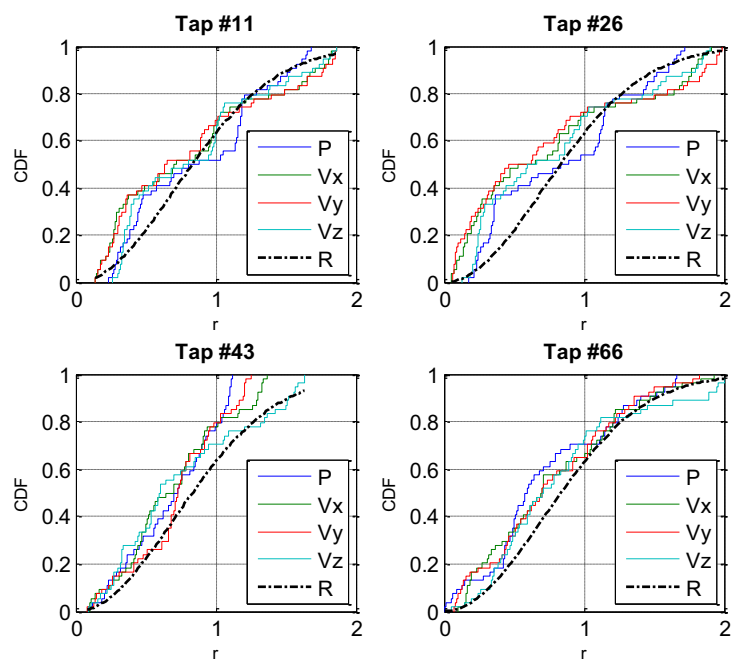

Fig. 11 CDFs of the amplitudes of four channel taps in all the channel impulse responses of a vector sensor receiver at 900m.

C. Wideband Channel Capacity

Using eq. (7) and with $N=12000$, average capacities of the vector sensor receiver and the scalar array receiver are calculated from measured data and are shown in Fig. 13. The two systems appear to have nearly the same capacity.

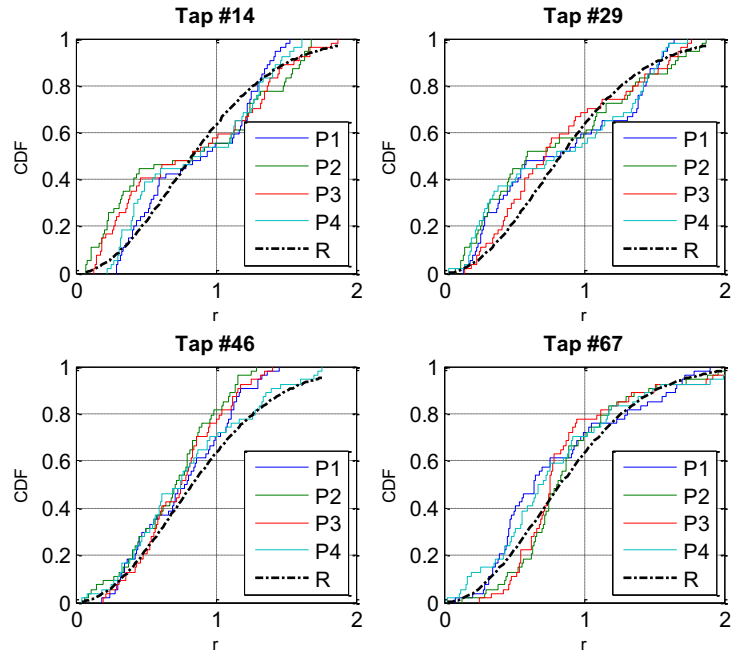

Fig. 12 CDFs of the amplitudes of four channel taps in all the channel impulse responses of a four-element scalar array receiver at 900m.

As a basic model, the average capacities of 1×4 wideband Rayleigh fading with the multi-exponential PDPs given in (9) and (10) are provided in Fig. 13. Each individual wideband Rayleigh channel is simulated according to $\sum_{l=0}^{L-1} a_l \delta[n-l]$, in which $L=150$ according to the measured data and a_l is zero-mean complex Gaussian whose power $E\{|a_l|^2\}$ is given by the associated PDP value $\Gamma[l]$. According to Fig. 13, wideband Rayleigh capacity seems to be closer to the measured wideband vector sensor capacity.

V. CONCLUSION

In this paper and using at-sea data, the channel statistics and capacity of a vector sensor receiver that measures the scalar and vector components of the acoustic field are investigated. It is observed that Rayleigh fading and multi-exponential power delay profile models accurately characterize the average capacity of acoustic particle velocity channels, measured by vector sensors. The results are useful for design and simulation of vector sensor communication systems in acoustic particle velocity channels. Capacity CDFs, noise distributions and possible noise

correlations will be discussed in another paper.

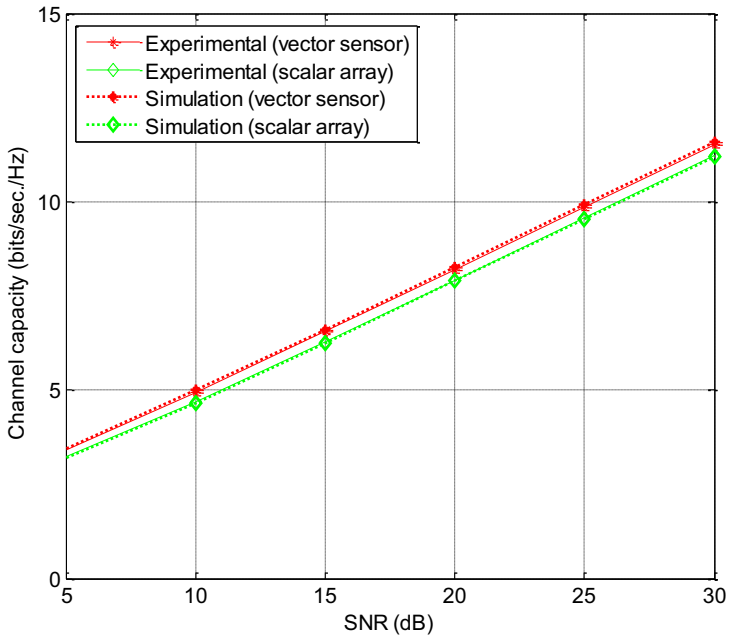

Fig. 13 Wideband channel capacities at 900m.

VI. ACKNOWLEDGEMENT

This work is supported in part by the National Science Foundation (NSF), Grant CCF-0830190.

REFERENCE

[1] A. Abdi and H. Guo, "A new compact multichannel receiver for underwater wireless communication networks," *IEEE Trans. Wireless Commun.*, vol. 8, pp. 3326-3329, 2009.

[2] A. Abdi, H. Guo and P. Sutthiwan, "A new vector sensor receiver for underwater acoustic communication," in *Proc. Oceans*, Vancouver, BC, Canada, 2007.

[3] D. B. Kilfoyle and A. B. Baggeroer, "The state of the art in underwater acoustic telemetry," *IEEE J. Oceanic Eng.*, vol. 25, pp. 4-27, 2000.

[4] M. Stojanovic, "High speed underwater acoustic communications," in *Underwater Acoustic Digital Signal Processing and Communication Systems*. R. S. H. Istepanian and M. Stojanovic, Eds, Boston, MA: Kluwer, pp. 1-35, 2002.

[5] A. Abdi, H. Guo, A. Song and M. Badiey, "An overview of underwater acoustic communication via particle velocity channels: Channel modeling and transceiver design," in *Proc. Meetings on Acoustics* (159th Meeting of Acoustical Society of America), Baltimore, MD, 2010.

[6] A. Song, A. Abdi, M. Badiey, and P. Hursky, "Experimental demonstration of underwater acoustic communication by vector sensors," *IEEE J. Oceanic Eng.*, vol. 36, pp. 454-461, 2011.

[7] H. Guo, A. Abdi, A. Song and M. Badiey, "Delay and Doppler spreads in underwater acoustic particle velocity channels," *J. Acoust. Soc. Am.*, vol. 129, pp. 2015-2025, 2011.

[8] A. Abdi and H. Guo, "Signal correlation modeling in acoustic vector sensor arrays," *IEEE Trans. Signal Processing*, vol. 57, pp. 892-903, 2009.

[9] M. Stojanovic, "On the relationship between capacity and distance in an underwater acoustic communication channel," *ACM SIGMOBILE Mobile Comput. Commun. Rev.*, vol. 11, pp. 34-43, 2007.

[10] D. E. Lucani, M. Stojanovic and M. Medard, "On the relationship between transmission power and capacity of an underwater acoustic communication channel," in *Proc. Oceans*, Kobe, Japan, 2008.

[11] P. King, R. Venkatesan and C. Li, "A study of channel capacity for a seabed underwater acoustic sensor network," in *Proc. Oceans*, Quebec City, QC, Canada, 2008.

[12] T.C. Yang, "Channel Q function and capacity," in *Proc. Oceans*, Washington, DC, pp. 273-277, 2005.

[13] M. Zatman and B. Tracey "Underwater acoustic MIMO channel capacity," in *Proc. Asilomar Conf. Signals, Systems, Computers*, Pacific Grove, CA, pp. 1364-1368, 2002.

[14] M. B. Porter, "The Makai experiment: High frequency acoustics," in *Proc. European Conf. Underwater Acoustic*, Carvoeiro, Portugal, 2006.

[15] J. G. Proakis, *Digital Communications*, 4th ed., McGraw-Hill, 2001.

[16] A. Radosevic, J. G. Proakis and M. Stojanovic, "Statistical characterization and capacity of shallow water acoustic channels," in *Proc. Oceans,* Bremen, Germany, 2009.

[17] T. S. Rappaport, *Wireless Communications: Principles and Practice*, 2nd ed., Prentice Hall PTR,

2002.

[18] A. Radosevic, D. Fertonani, T. Duman, J. G. Proakis, and M. Stojanovic, "Capacity of MIMO systems in shallow water acoustic channels," in *Proc. Asilomar Conf. Signals, Systems, Computers*, Pacific Grove, CA, pp. 2164-2168, 2010.

[19] D. Tse and P. Viswanath, *Fundamentals of Wireless Communication*. Cambridge University, 2005.

[20] E. Telatar, "Capacity of multi-antenna Gaussian channels," *European Trans. Telecommun.*, vol. 10, pp. 585-595, 1999.

[21] M. Kang, and M.S. Alouini, "Capacity of MIMO Rician channels,", *IEEE Trans. Wireless Comm.* vol. 5, pp. 112-122, 2006.

[22] A. Paulraj, R. Nabar and D. Gore, *Introduction to Space-time Wireless Communications*. Cambridge University, 2003.

[23] A. F. Molisch, *Wireless Communications*. Wiley-IEEE, 2005.